Available online at www.sciencedirect.com
SCIENCE DIRECT
Surface Science 600 (2006) 2372–2378
SURFACE SCIENCE
www.elsevier.com/locate/susc

Initial oxidation kinetics and energetics of $Cu_{0.5}Au_{0.5}$ (001) film investigated by in situ ultrahigh vacuum transmission electron microscopy

Liang Wang [a,*], Guang-Wen Zhou [b], Jeffrey A. Eastman [b], Judith C. Yang [a]

[a] *Department of Materials Science and Engineering, University of Pittsburgh, Pittsburgh, PA 15261, USA*
[b] *Materials Science Division, Argonne National Laboratory, Argonne, IL 60439, USA*

Received 5 September 2005; accepted for publication 31 March 2006
Available online 27 April 2006

Abstract

The initial oxidation behavior of $Cu_{0.5}Au_{0.5}$ (001) thin film was investigated by in situ ultrahigh vacuum transmission electron microscopy to model nano-oxidation of alloys with one active component and one noble component. The formation of irregular-shaped octahedron Cu_2O islands with cube-on-cube crystallographic orientation to the substrate film was observed at all temperature studied. The energetics of Cu_2O nucleation for Cu and $Cu_{0.5}Au_{0.5}$ oxidation was compared. $Cu_{0.5}Au_{0.5}$ oxidation has lower nucleation activation energy due to the reduced mismatch strain between Cu_2O and $Cu_{0.5}Au_{0.5}$ films. On the other hand, the reaction kinetics for $Cu_{0.5}Au_{0.5}$ alloy oxidation is slower due to the higher diffusion activation energy of Cu.

Keywords: Cu–Au alloy; Cu_2O; Nano-oxidation; In situ UHV–TEM; Thin film; Surface

1. Introduction

Classic investigations of the oxidation behavior of pure metals are mostly based on thermogravimetric analysis (TGA), which measures weight changes but not structural changes. Classic models of oxidation usually assume uniform oxide film growth. However it is well known that many metals form oxide islands (e.g., Ni [1,2], Pd [3], Fe [4–6] and Ti [7]) at the early stage of oxidation, and that later the oxide islands coalesce into an oxide scale. The nucleation and growth processes of oxides are particularly important due to their impact on understanding diverse materials problems, from passivation properties [8,9], to the synthesis of self-assembled nano-oxide structures for optical [4], magnetic [5] or catalytic performance [10,11].

Many elegant surface science studies have been performed to reveal the interaction of oxygen gas with a bare metal surface [3,12–14], but these studies only extend to a few monolayers. Most bulk oxidation studies focus on the growth of the thermodynamically stable oxide, that are a few microns and thicker. By using in situ ultrahigh vacuum (UHV) transmission electron microscopy (TEM), information inaccessible to both surface science study and traditional oxidation methods can be ascertained. The previous work of Yang et al. [15–18] and Zhou et al. [7,16,18], using Cu as a model system, clearly demonstrated that heteroepitaxial concepts, used for film growth, also describes surprisingly well the nano-oxidation of metals and a vast range of information is yielded regarding dynamics of oxide formation, size and shape evolution of nano-oxides, temperature, pressure and crystal orientation effects, as well as the environmental stability of the oxide.

However, most engineered materials are alloys that they serve under harsh environment where oxidation and corrosion are among the major mechanisms causing device

* Corresponding author. Present address: Department of Materials Science and Engineering, University of Illinois at Urbana-Champaign, IL 61801, USA.
E-mail address: lwang20@uiuc.edu (L. Wang).

0039-6028/$ - see front matter © 2006 Elsevier B.V. All rights reserved.
doi:10.1016/j.susc.2006.03.044

failure. Hence, it is critical to understand how the nucleation and growth processes of the oxides during oxidation of an alloy are affected by the presence of secondary elements, such as preferred nucleation position in multiphase system, composition of the nucleus of a system with more than one active alloying elements, and the redistribution of alloy elements during oxide growth. In this paper, we report in situ studies of the oxidation behavior of a copper-based alloy and try to resolve the effect of inert atom species on oxidizing species. We use Cu50 at%Au ($Cu_{0.5}Au_{0.5}$) as a model system because of the in-depth understanding of Cu oxidation dynamics and that both the clean and the oxygen modified surface structures of Cu–Au alloys have been widely investigated by low-energy ion scattering [19], computer simulation [20], X-ray scattering [21], Auger electron spectroscopy [22], low-energy electron diffraction [23], etc. Since Au is stable and miscible to Cu at the composition and temperature range which we investigated, only Cu_2O is expected to form on the Cu–Au alloy. Nevertheless, many differences exist between Cu and Cu–Au that are pivotal to surface processes and, hence, will impact nano-oxidation dramatically. These differences include: (1) lattice constant (thus lattice mismatch and strain energy); (2) surface energy; (3) segregation of Au to surface; (4) diffusion of Au and Cu during oxidation that affects kinetics of oxidation of Cu; (5) limited supply of Cu that may lead to self-limited growth of oxide; and (6) dilute effect of Au on Cu activity.

2. Experiment

The microscope used for this experiment is a modified JEOL 200CX TEM. These modifications permit the introduction of gases directly into the microscope column through a manually controlled leak valve and in situ resistance heating up to 1000 °C. A UHV chamber is attached to the middle of the column, where the base pressure is $<10^{-9}$ torr with liquid helium cryoshroud. For more details about the experimental apparatus, see McDonald et al. [24].

Single crystal $Cu_{0.5}Au_{0.5}$ (0 0 1) film with thickness of 90 nm was grown on irradiated NaCl (0 0 1) in a co-sputtering system, where the base pressure was 10^{-8} torr. Cu and Au were deposited simultaneously with a substrate temperature of 270 °C and an Ar pressure of 5 mtorr. After deposition the film was annealed at the same temperature for half an hour. The film composition and thickness were calibrated by Rutherford-back scattering. The film was then cut into desired size and removed from the substrate by floatation in deionized water, washed and mounted on a specially prepared Si holder. The sample was annealed in situ at ~800 °C for 10 min to increase the homogeneity of the film. Scientific grade O_2 gas of 99.999% purity was admitted into the column of the microscope with a partial pressure in the range between 5×10^{-5} and 760 torr. Oxidation was carried out at a temperature range from 550 °C to 750 °C with constant O_2 partial pressure at 5×10^{-4} torr. Ex situ nanobeam electron diffraction (NED) was performed on a JEOL 2010F electron microscope (See Ref. [25] for electron ray diagram for NED mode). Diffraction patterns were recorded on imaging plates. The topology of the oxide islands were analyzed by a Digital Instrument dimension 3100 atomic force microscope (AFM) in tapping mode. TEM negatives taken by JEOL 200CX microscope were digitized with a Leafscan™ 45, and the software package NIH ImageJ™ was used to determine the cross-section area of the oxide islands.

3. Results and discussions

3.1. Structure of the film before oxidation

Below T_C (~410 °C), $Cu_{0.5}Au_{0.5}$ film assumes an ordered $L1_0$ tetragonal structure. Because $a = b \neq c$, there are two possible in-plane configurations–c axis normal to or c axis in the film plane, which can be distinguished by electron diffraction. Fig. 1(b) is an electron diffraction pattern of the film at room temperature showing the single crystal nature of the film. Both the four-fold symmetry and the extinction of {1 0 0} spots indicate that the c axis is normal to the film. Furthermore, no diffraction spot from an oxide are visible in Fig. 1(b) indicating that the film surface does not form a noticeable amount of native oxide, as compared to bare Cu (0 0 1) [7]. Upon heating to ~410 °C, the {1 1 0} type superlattice spots gradually disappear demonstrating an order to disorder transition at this point. Fig. 1(a) is a bright field (BF) TEM image of the film at 550 °C. Fig. 1(c) shows a diffraction pattern of the disordered FCC structure along (0 0 1) zone axis at 550 °C. All oxidation reported in this paper were carried out above the T_C.

Cu–Au alloy surface has been studied extensively both experimentally and theoretically. For clean (0 0 1) $Cu_{1-x}Au_x$ thin film, the Au atoms segregate to the topmost layer because of its lower surface energy (See Refs. [20,26,27]), while Cu enriches the second layer to maximize

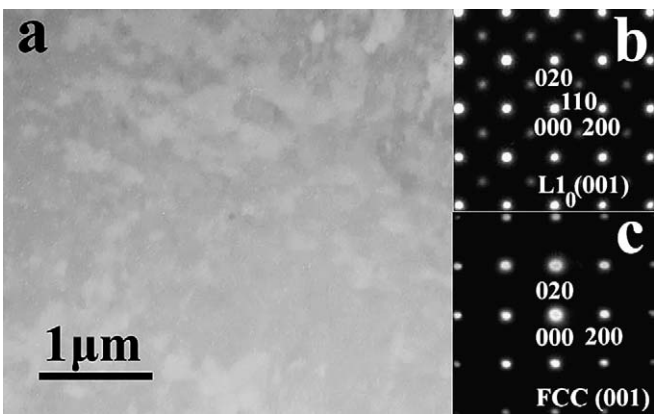

Fig. 1. (a) BF TEM image of the $Cu_{0.5}Au_{0.5}$ (0 0 1) film at 550 °C, (b) diffraction pattern from the film at room temperature which shows ordered $L1_0$ structure, (c) diffraction pattern of the film at 550 °C with disordered FCC structure.

the short-range ordering [28], then Au-rich again, and so forth. This configuration results in a layer-by-layer structure consisting of alternating Au-rich and Cu-rich (0 0 1) layers. The depth of the oscillatory concentration profile is highly temperature dependent [20]. Naturally, below T_C, this oscillatory concentration profile extends throughout the film in $Cu_{0.5}Au_{0.5}$. Above T_C, the depth decreases as temperature increases, since the entropy contribution to the free energy favors a random arrangement. Nevertheless, Au still has a higher concentration in the topmost layer than the bulk even above T_C. The significance of the atom configuration to the oxide nucleation process will be discussed next.

3.2. Oxide nucleation

After admitting oxygen gas, the nuclei appear after an incubation time (τ_0) ranging from tens of seconds to several minutes depending on the reaction temperature, oxygen pressure and the film composition. During this incubation time, O_2 molecules striking the film dissociate and diffuse on the surface. However, since we speculate that the clean Cu–Au surface is rich in Au, it is relatively inert toward oxygen adsorption and dissociation especially at low temperature when Au concentration on the surface is higher [29]. Previous studies [29–31] demonstrate that the oxygen adsorption and dissociation is accomplished by the out-diffusion of Cu atoms to the top layer to form Cu–O bonds and Au in-diffusion driven by the greater affinity of O for Cu than for Au. Further exposure of the film to O_2 increases O atom concentration on the metal surface. The oxygen saturated overlayer subsequently facilitates nucleation of Cu_2O when the chemical potential of oxygen reaches a critical point (as determined by temperature and Cu concentration). Our experimental results show that at the oxygen partial pressure of 5×10^{-4} torr, τ_0 decreases as the reaction temperature increases, e.g., $\tau_0 = 4$ min for 600 °C oxidation, $\tau_0 = 3$ min for $T = 650$ °C, and $\tau_0 = 50$ s when $T = 700$ °C. Compared with its Cu (0 0 1) counterparts (where $\tau_0 = 1.5$ min for 600 °C oxidation, $\tau_0 = 1$ min for 650 °C oxidation, and $\tau_0 < 1$ min for 700 °C), $Cu_{0.5}Au_{0.5}$ (0 0 1) has a longer oxidation incubation time. The longer incubation time is a result that oxygen chemisorption requires much longer time on the Cu–Au surface than on pure Cu because it involves both the out-diffusion of Cu and in-diffusion of Au. As the temperature increases, the higher mobility of the atoms allows more rapid adsorption of oxygen and thus the incubation time shortens with increasing temperature.

After the first nucleus appears, the nuclei density increases with time until a saturation density is reached and then it will decrease as islands start to coalesce. Nucleation processes can be characterized by an initial nucleation rate (nucleation density change per unit time) [32]. For the oxidation of $Cu_{0.5}Au_{0.5}$ film, the saturation density was reached surprisingly fast. For example, at 550 °C and $P(O_2) = 5 \times 10^{-4}$ torr, the saturation density was reached for only a 30 s after nucleation started. In Section 3.4 this phenomenon will be addressed when we discuss the nucleation energetics.

3.3. Morphology evolution

The primitive cell of Cu_2O is cubic with space group *Pn-3 m* ($a = 0.422$ nm), and contains two oxygen atoms and four copper atoms [33]. The oxygen atoms form a body centered cubic structure, while the copper atoms partially occupy the interstitial positions in an alternating pattern. Fig. 2(a) is a set of BF TEM images showing the growth sequence of a Cu_2O island at 600 °C. Actually, the same shape evolution was observed for all the temperatures we investigated. The cross-shaped pattern in the first three images indicates that the Cu_2O has a pyramidal-shape. NED [Fig. 2(b)] was taken by parallel electron probe with a beam size of ~100 nm illuminating only the pyramid-shaped oxide island. The strong diffraction spots in Fig. 2(b) are those from the Cu–Au film. Associated with each strong spot are satellite diffraction spots from the oxide which is characteristic of double diffraction. One major diffraction spot and its satellite spots are enlarged in the inset of Fig. 2(b). The strong diffraction spot in the center is the primary diffraction from Cu. The surrounding spots are those of Cu_2O generated by double diffraction. The appearance of double diffraction demonstrates that the oxide island has not yet penetrated through the film. The cube-on-cube crystallographic orientation of Cu_2O (0 0 1)//$Cu_{0.5}Au_{0.5}$ (0 0 1) and Cu_2O [1 0 0]//$Cu_{0.5}Au_{0.5}$ [1 0 0] could also be inferred from the diffraction pattern. Since NED was done at room temperature, very weak {1 1 0} superlattice reflections from the substrate also show up. NED was utilized here instead of selected area electron

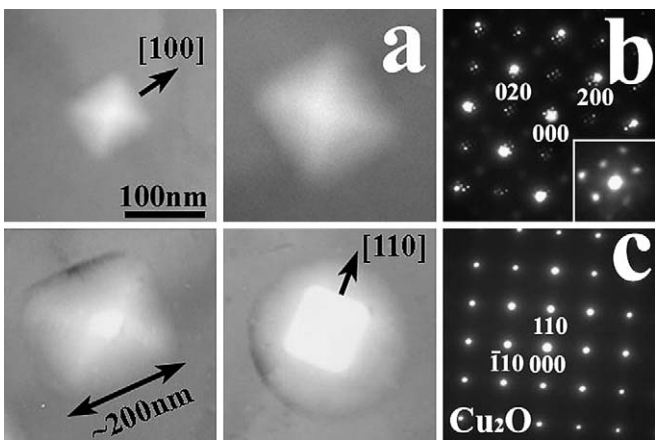

Fig. 2. (a) Time-lapse BF TEM of an oxide island oxidized at 600 °C showing the shape evolution, the facets of the oxide island are along ⟨1 0 0⟩ directions before penetration through the film and along ⟨1 1 0⟩ directions after penetration; (b) NED shows double diffraction from the film and oxide due to the overlapping of each other. The inset is an enlarge view of the satellite diffraction spots around a strong reflection from the film. (c) NED from the penetrated part of the oxide island showing diffraction pattern from only Cu_2O.

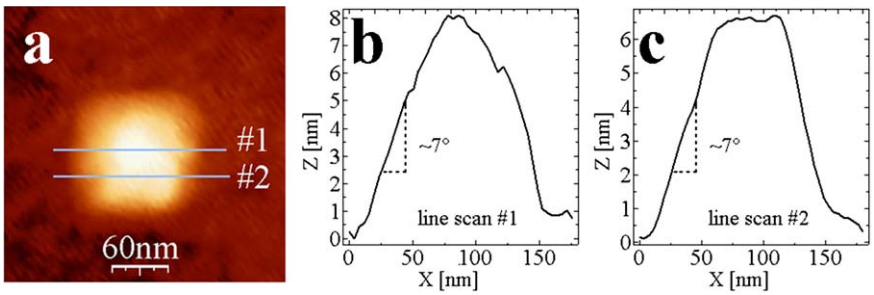

Fig. 3. (a) AFM image of one Cu_2O island, (b) line scan across the center and (c) off center. Both (b) and (c) show the inclination angle of the bounding plane is around 7°.

diffraction to reveal weak diffraction from nanoarea oxide islands that would have been otherwise overshadowed by the strong diffraction from the metal film. In the last two micrographs of Fig. 2(a), an area with bright contrast is also observed to form at the center of the island. NED from only this central area [Fig. 2(c)] has only the Cu_2O diffraction spots indicating the penetration of oxide through the metallic film when the pyramid reaches the critical size of ~200 nm. Fig. 2 also reveals several other distinct configurations of the island. The edges of Cu_2O pyramid before penetration are along $\langle 100 \rangle$ directions; After penetration the oxide maintains square-shape but the edges are now along $\langle 110 \rangle$ directions. The reason of the shape transition is not clear now, however, it must be related to the reduction in total energy of the system. As the island penetrates through the film, an extra oxide surface, thus extra surface energy, is created which increases the total energy of the island. The system may change its shape to accommodate the energy change. In order to obtain information that is comparable to bulk material oxidation, we discuss in this paper only the regime before oxide penetration occurs.

In order to determine the shape of the Cu_2O islands in three dimensions, we first use AFM to ascertain the topology of the Cu_2O island. Fig. 3(a) shows a typical AFM image of the island. Fig. 3(b) and (c) are height profiles passing through the center (line scan #1) and off the center (line scan #2) of the oxide island along the marked lines in $\langle 100 \rangle$ direction. A triangular-shaped height profile through the center plus trapezoid-shaped profile off the center reveal the pyramid shape topology of the island. Fig. 3(b) and (c) also show that the four facets bounding the pyramid inclines with ~7° angle to (001) film surface. Since these facets also intersect (001) plane at $\langle 100 \rangle$ direction, we identified them as {108}.

The maximum size of the Cu_2O pyramid before penetration is ~200 nm [Fig. 2(a)]. As shown in the structure model of Fig. 4(a), the four Cu_2O/Cu–Au interfaces form ~42° angle to (001) and they intersect (001) at $\langle 001 \rangle$ type directions. The only low index plane with these configurations is {110}. The angle formed by {110} and {100} planes are 45°; this angle is used in the following calculation. From above analyses we determine the island to be an irregular-shaped octahedron [Fig. 4(b)]. The top of the octahedron is enclosed by four {108} facets and the Cu_2O/Cu–Au interfaces are {110} type. The volume of the island is $V = \frac{9}{48} l^3$ and the projected area is $A = l^2$, where l is the edge length. This structural model demonstrates a 3D island growth mode.

3.4. Energetics of nucleation

The overall free energy (ΔG) for oxidation is determined by molar Gibbs free energy of formation of Cu_2O (ΔG^f), surface energy changes, interfacial energy change, and strain energy in the oxide as

$$\Delta G = \Delta G^f \frac{V}{V_o} + (\gamma_o A_o - \gamma_m A_m + \gamma_{o/m} A_{o/m}) + \frac{E}{1-v} \varepsilon^2 V \quad (1)$$

where V and V_o are the volume and molar volume of Cu_2O, respectively. γ_o, γ_m, and $\gamma_{o/m}$ are the surface energy of oxide, metal and interaction contribution to the interfacial energy [34]. At present, the experimental values of surface and interface energy of metal-oxide are usually not

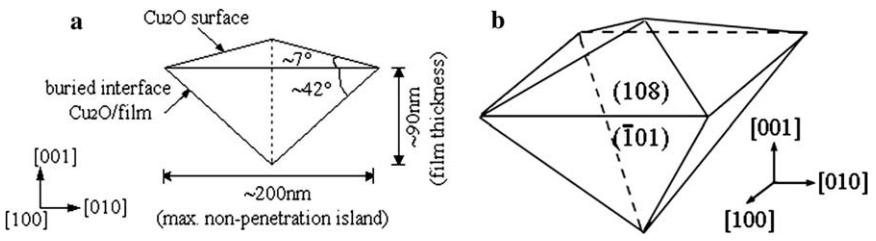

Fig. 4. Three dimension structural model of the Cu_2O islands. (a) two dimension projected view from [100] direction, (b) three dimension view showing the irregular octahedron pyramids structure.

available, but to a good approximation γ_m is assumed to equal to γ_{Cu} because in both cases oxide nucleates on oxygen saturated Cu rich surface (see 3.2. for details). $\gamma_{o/m}$ is also assumed to equal to its Cu (001) counterpart given that there is no significant segregation of Au to the interface. A_o, A_m, and $A_{o/m}$ correspond to the area of oxide, metal and interface. From the structure model of the islands we know that $A_o = l^2/\cos 7°$, $A_m = l^2$ and $A_{o/m} = l^2/\cos 45°$. The last term in Eq. (1) is the elastic strain energy stored in the oxide. E, ε and v are Young's modulus, strain and Poisson's ratio, respectively.

From classic nucleation theory we know that the critical nucleus size, l^*, and the nucleation barrier, ΔG^*, are

$$l^* \propto -\frac{\Gamma}{\frac{\Delta G^f}{V_o} + \frac{E}{1-v}\varepsilon^2} \quad \text{and} \quad \Delta G^* \propto \frac{\Gamma^3}{\left(\frac{\Delta G^f}{V_o} + \frac{E}{1-v}\varepsilon^2\right)^2} \tag{2}$$

where $\Gamma = \gamma_o/\cos 7° - \gamma_m + \gamma_{o/m}/\cos 45°$. Standard thermodynamic data [35] shows that

$$\Delta G^f = -166500 + (122.2 - 16.63\ln[Cu])T \tag{3}$$

where [Cu] is the activity of copper, T is reaction temperature in K. The activity of Cu is 1 in pure state and 0.5 in $Cu_{0.5}Au_{0.5}$ under ideal solution assumption. ΔG^f is then calculated to be −53.7 KJ/mol for pure Cu oxidation and −43.1 KJ/mol for $Cu_{0.5}Au_{0.5}$ oxidation. The lattice mismatch strain, ε, in pure Cu is 16.8%, while in $Cu_{0.5}Au_{0.5}$ $\varepsilon = 10.5\%$ [since $a(Cu_2O) = 4.22$ Å, $a(Cu) = 3.61$ Å, $a(Au) = 4.02$ Å and by Vegard's law $a(Cu_{0.5}Au_{0.5}) = 3.82$ Å]. Plug in the value of E (=30 GPa) and v (=0.455) [36], we have $l^*_{Cu-Au} = 0.64 \cdot l^*_{Cu}$ and $\Delta G^*_{Cu-Au} = 0.40 \cdot \Delta G^*_{Cu}$. Hence, nucleation of Cu_2O on $Cu_{0.5}Au_{0.5}$ surface requires smaller critical nuclei size and lower activation energy (reduced by 60%] than on bare Cu surface. In Section 3.2 we mentioned that $Cu_{0.5}Au_{0.5}$ oxidation shows a surprisingly fast nucleation rate as compared to that of Cu oxidation. Our energetics argument predicts the exact behavior that we observed. Since nucleation rate is proportional to $\exp(-\Delta G^*/kT)$, 60% decreases in ΔG^* dramatically increase the nucleation rate so that no nucleation event could be recorded during the experiment.

Actually the Gibbs free energy of formation term ($\Delta G^f/V_o$) and the strain energy term $\left(\frac{E}{1-v}\varepsilon^2\right)$ make opposite contribution to the overall Gibbs free energy change when Au is added to the system. Activity of Cu reduces because of Au dilution effect, so from Eq. (3) we know that ΔG^f in $Cu_{0.5}Au_{0.5}$ is less negative and thus the overall Gibbs free energy for oxidation increases. But since ε for $Cu_2O/Cu_{0.5}Au_{0.5}$ is smaller, the strain energy contribution decreases overall Gibbs free energy for nucleation. The positive contribution from $\left(\frac{E}{1-v}\varepsilon^2\right)$ term exceeds the negative contribution from ($\Delta G^f/V_o$) term and a smaller activation free energy of nucleation (ΔG^*) results.

3.5. Oxide growth kinetics

The oxide growth kinetics is characterized by the cross-section area change as a function of exposure time. It is phenomenologically described in classical mean-field theory that the growth of surface features follow scaling law such that [17,37,38]

$$A(t) = C \cdot (t - t_0)^n \tag{4}$$

where C is the area growth factor, t_0 is the time at which island nucleates, t is the lapse of time from oxygen exposure, and n is the power law dependence. Fig. 5(a)–(c) are three TEM micrographs showing islands growth at 650 °C. The images were acquired at 5 min, 10 min and 17 min. In Fig. 5c, island 3 already penetrated through the film revealed by the characteristic white contrast in the center. Fig. 6 is a plot of the average $A(t)$ versus t. Discrete symbols are the experimental data and solid line correspond to theoretical fitting to Eq. (4). By taking logarithm to Eq. (4) and making a linear fit to the data, n could be determined to be 0.99 ± 0.02. Thus, it is reasonable to believe the islands grow linearly with reaction time, and C could then be calculated to be 0.0025 ± 0.0001 μm^2/min. The oxidation kinetics of $Cu_{0.5}Au_{0.5}$ film at other investigated temperatures have the same linear power law dependence but with different C

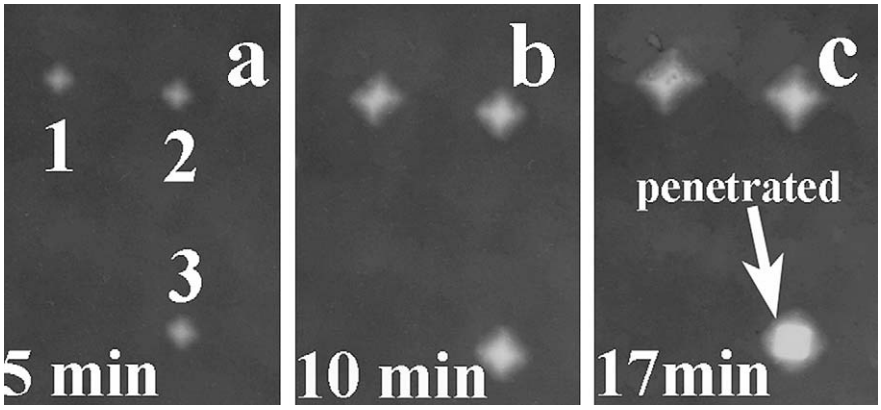

Fig. 5. Typical BF TEM images of $Cu_{0.5}Au_{0.5}$ (001) oxidation at 650 °C for times (a) $t = 5$ min, (b) $t = 10$ min and (c) $t = 17$ min.

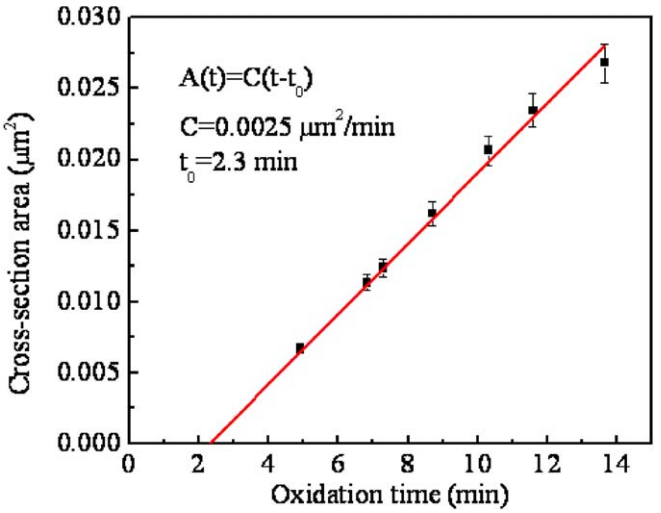

Fig. 6. Plot of average Cu_2O islands cross-section area as a function of oxidation time. The experimental data was fitted by linear growth law with area growth factor C and incubation time t_0 showing in the plot.

(e.g., $C = 0.11 \pm 0.01$ and $0.0005 \pm 0.0002\ \mu m^2/min$ for 700 °C and 600 °C oxidation, respectively). Generally, as the temperature increases, C also increases. The area growth factor C for $Cu_{0.5}Au_{0.5}$ oxidation at 600 °C could be converted to volume growth factor as $C' = 2.1 \times 10^3\ nm^3/min$. The volume growth factor for Cu (001) oxidation at 600 °C [16] is $1.2 \times 10^5\ nm^3/min$ which is almost two magnitudes larger than the $Cu_{0.5}Au_{0.5}$ case. The reason for the much slower growth kinetics is because in Cu (001) oxidation there is no need for Cu transportation, and the only rate-limiting step is oxygen surface diffusion. While in Cu–Au oxidation, diffusion of Cu in Cu–Au alloy has an activation energy of ~1.6 eV [39,40] and may slow the reaction. In fact in the case of Cu–Au alloy oxidation, since there is only finite amount of Cu and there will be many Cu_2O particles drawing Cu atoms from the matrix, as the islands grow bigger the area from which they absorb Cu will overlap. When this happens, the matrix could not provide sufficient supply of Cu then a self-limiting growth law results. Experimentally, the self-limiting growth occurs at a later stage of oxidation and is beyond the scope of this paper.

4. Conclusion

$Cu_{0.5}Au_{0.5}$ (001) thin film was used as a model system for the characterization of alloy nano-oxidation by in situ UHV–TEM. The addition of inert Au into Cu greatly modified the oxidation kinetics and energetics of Cu. Au reduces the oxidation kinetics of Cu. Oxidation of $Cu_{0.5}Au_{0.5}$ surface requires a longer incubation time, since longer time is needed to establish an oxygen chemisorbed overlayer on clean Cu–Au surface with inert Au-rich layer on top. The volume growth rate of Cu_2O islands on $Cu_{0.5}Au_{0.5}$ (001) is two magnitudes slower than on Cu (001) surface at the same temperature, because diffusion of Cu in Cu–Au alloy is slow and probably is the rate-controlling step. However, addition of Au to the film decreases lattice mismatch between Cu_2O and the substrate film and hence lowers the oxide nucleation activation energy. The shape of the Cu_2O islands is deduced to be irregular octahedron based on AFM and TEM observations. Our results indicate that even for the simplest alloy system, such as Cu–Au, with one oxidizing component and one noble component, the oxidation behavior can be significantly different from that of the pure component. Further study of alloys oxidation with two or even more active species should consider all the factors that may alter the reaction kinetics/energetics such as surface structure, lattice mismatch strain, alloying effects on activity, surface structure and energy, interfacial strain energies, etc.

Acknowledgments

This research project is funded by National Science Foundation (#9902863). The experiments were carried out in the Center for Microanalysis of Materials, University of Illinois at Urbana-Champaign, which is partially supported by the U.S. Department of Energy under grant DEFG02-91-ER45439. The authors kindly thank I. Petrov, R. Twesten, K. Colravy, S. MacLaren, M. Marshall, J.G. Wen, and T. Banks (University of Illinois) for their help. Discussions with B.Q. Li (University of Illinois) are kindly acknowledged.

References

[1] P. Marikar, M.B. Brodsky, C.H. Sowers, N.J. Zaluzec, Ultramicroscopy 29 (1989) 247.
[2] P.H. Holloway, J.B. Hudson, Surf. Sci. 43 (1974) 141.
[3] K. Thurmer, E. Williams, J. Reutt-Robey, Science 297 (2002) 2033.
[4] S. Aggarwal, A.P. Monga, S.R. Perusse, R. Ramesh, V. Ballarotto, E.D. Williams, B.R. Chalamala, Y. Wei, R.H. Reuss, Science 287 (2000) 2235.
[5] S. Aggarwal, S.B. Ogale, C.S. Ganpule, S.R. Shinde, V.A. Novikov, A.P. Monga, M.R. Burr, R. Ramesh, V. Ballarotto, E.D. Williams, Appl. Phys. Lett. 78 (2001) 1442.
[6] S.R. Shinde, A.S. Ogale, S.B. Ogale, S. Aggarwal, V. Novikov, E.D. Williams, R. Ramesh, Phys. Rev. B 64 (2001) 035408.
[7] G.W. Zhou, Thesis, University of Pittsburgh, 2003.
[8] N.P. Padture, M. Gell, E.H. Jordan, Science 296 (2002) 280.
[9] A.G. Evans, D.R. Mumm, J.W. Hutchinson, G.H. Meier, F.S. Pettit, Prog. Mater. Sci. 46 (2001) 505.
[10] H. Over, Y.D. Kim, A.P. Seitsonen, S. Wendt, E. Lundgren, M. Schmid, P. Varga, A. Morgante, G. Ertl, Science 287 (2000) 1474.
[11] B. Delmon, in: G. Ertl, H. Knözinger, J. Weitkamp (Eds.), Handbook of Heterogeneous Catalysis, Wiley-VCH, New York, USA, 1997, p. 264.
[12] D.J. Coulman, J. Wintterlin, R.J. Behm, G. Ertl, Phys. Rev. Lett. 64 (1990) 1761.
[13] L. Eierdal, F. Besenbacher, E. Laegsgaard, I. Stensgaard, Surf. Sci. 312 (1994) 31.
[14] C.I. Carlisle, T. Fujimoto, W.S. Sim, D.A. King, Surf. Sci. 470 (2000) 15.
[15] J.C. Yang, D. Evan, L. Tropia, Appl. Phys. Lett. 81 (2002) 241.
[16] G.W. Zhou, J.C. Yang, Phys. Rev. Lett. 89 (2002) 106101.
[17] J.C. Yang, M. Yeadon, B. Kolasa, J.M. Gibson, Appl. Phys. Lett. 70 (1997) 3522.
[18] G.W. Zhou, J.C. Yang, Appl. Surf. Sci. 210 (2003) 165.

[19] T.M. Buck, G.H. Wheatley, L. Marchut, Phys. Rev. Lett. 51 (1983) 43.
[20] J. Tersoff, Phys. Rev. B 42 (1990) 10965.
[21] H. Reichert, P.J. Eng, H. Dosch, I.K. Robinson, Phys. Rev. Lett. 74 (1995) 2006.
[22] S. Mroz, Prog. Surf. Sci. 59 (1998) 323.
[23] H. Over, G. Gilarowski, H. Niehus, Surf. Sci. 381 (1997) L619.
[24] M.L. Mcdonald, J.M. Gibson, F.C. Unterwald, Rev. Sci. Instrum. 60 (1989) 700.
[25] M. Gao, J.M. Zuo, R.D. Twesten, I. Petrov, L.A. Nagahara, R. Zhang, Appl. Phys. Lett. 82 (2003) 2703.
[26] M. Polak, L. Rubinovich, Surf. Sci. Rep. 38 (2000) 129.
[27] U. Bardi, Rep. Prog. Phys. 57 (1994) 939.
[28] I.K. Robinson, P.J. Eng, Phys. Rev. B 52 (1995) 9955.
[29] G.W. Graham, Surf. Sci. 137 (1984) L79.
[30] H. Niehus, C. Achete, Surf. Sci. 289 (1993) 19.
[31] S. Nakanishi, K. Kawamoto, N. Fukuoka, K. Umezawa, Surf. Sci. 261 (1992) 342.
[32] J.C. Yang, M. Yeadon, B. Kolasa, J.M. Gibson, Scripta Mater. 38 (1998) 1237.
[33] R.W.G. Wychoff, second ed.Crystal Structures, vol. 1, Wiley, New York, 1963.
[34] L.P.H. Jeurgens, W.G. Sloof, F.D. Tichelaar, E.J. Mittemeijer, Phys. Rev. B 62 (2000) 4707.
[35] D.R. Gaskell, Introduction to metallurgical thermodynamics, second ed., McGraw-Hill Book Company, New York, 1981.
[36] P.R. Markworth, X. Liu, J.Y. Dai, W. Fan, T.J. Marks, R.P.H. Chang, J. Mater. Res. 16 (2001) 2408.
[37] F. Family, P. Meakin, Phys. Rev. Lett. 61 (1988) 428.
[38] M. Zinkeallmang, L.C. Feldman, M.H. Grabow, Surf. Sci. Rep. 16 (1992) 377.
[39] B. Straumal, E. Rabkin, W. Gust, B. Predel, Acta Metallurgica Et Materialia 43 (1995) 1817.
[40] K.N. Tu, B.S. Berry, J. Appl. Phys. 43 (1972) 3283.